



APPLIED SCIENCES AND ENGINEERING

An ultrathin membrane mediates tissue-specific morphogenesis and barrier function in a human kidney chip

Xingrui Mou¹, Jessica Shah^{1†}, Yasmin Roye¹, Carolyn Du¹, Samira Musah^{1,2,3,4,5*}

Organ-on-chip (OOC) systems are revolutionizing tissue engineering by providing dynamic models of tissue structure, organ-level function, and disease phenotypes using human cells. However, nonbiological components of OOC devices often limit the recapitulation of in vivo-like tissue-tissue cross-talk and morphogenesis. Here, we engineered a kidney glomerulus-on-a-chip that recapitulates glomerular morphogenesis and barrier function using a biomimetic ultrathin membrane and human-induced pluripotent stem cells. The resulting chip comprised a proximate epithelial-endothelial tissue interface, which reconstituted the selective molecular filtration function of healthy and diseased kidneys. In addition, fenestrated endothelium was successfully induced from human pluripotent stem cells in an OOC device, through in vivo-like paracrine signaling across the ultrathin membrane. Thus, this device provides a dynamic tissue engineering platform for modeling human kidney-specific morphogenesis and function, enabling mechanistic studies of stem cell differentiation, organ physiology, and pathophysiology.

INTRODUCTION

Organ-on-chip (OOC) technology integrates techniques from materials science, tissue engineering, and cell and developmental biology to produce in vitro platforms that mimic the physiological environment of human organs (1–4). OOCs are compact—about the size of a universal serial bus (USB) flash drive—and contain fluidic microchannels that support cell culture and tissue formation. Dynamic fluid flow is used to apply shear stress to cells to stimulate mechanosensitive gene expression and regulate cell fate decisions, proliferation, maturation, and signaling (5). The orientation of the fluidic microchannels can be designed to match the in vivo tissue organization of the organ of interest, with neighboring channels forming tissue-tissue interfaces that mimic those in the physiological environment. For example, the blood-brain barrier (6), lung alveoli (7), and the glomerular filtration barrier (8–11) were modeled by stacking two microchannels separated by a porous membrane to facilitate cell adhesion. OOC systems have been applied to drug screening (12, 13), disease modeling (14, 15), and developmental biology research (5).

Since the seminal 2010 report by Huh *et al.* (16), the field of OOC systems has grown rapidly as OOCs provide in vitro models that avoid interspecies differences that limit the utility of animal models for understanding human biological responses in disease research and therapeutic discovery. For example, OOCs can use human stem cell differentiation techniques to generate human-specific organ models for preclinical studies, while over 90% of drug candidates that pass animal model-based preclinical studies fail in human clinical trials (17), OOCs developed with human cells have demonstrated

improved prediction of human responses and increased success rates in drug development (18, 19). Recognizing the groundbreaking advantages of OOCs, the US Food and Drug Administration (FDA) approved OOCs for use as preclinical study models as part of the FDA Modernization Act 2.0 passed in 2022, eliminating the mandate for animal testing before in-human clinical trials (20).

However, nonbiological materials in OOCs often limit their performance. For example, the membranes separating fluidic channels in OOCs are typically composed of polymers such as polydimethylsiloxane (PDMS) or polycarbonate (PC) which are used due to their mechanical integrity under fluid flow and biocompatibility, but these polymers result in permanent nondegradable membranes, which are orders of magnitude thicker than basement membranes in human organs. PDMS and PC membranes used in OOCs have been ~30- to 50- μm thick (21, 22), while basement membranes in human organs are often less than 1- μm thick (23, 24). Creating ultrathin PDMS membranes for OOCs (25) requires specialized and cost-prohibitive equipment and techniques (e.g., reactive-ion etching with specialized gases), which presents notable manufacturing barrier. In addition, the inert nature of PDMS, PC, and other synthetic polymers results in a permanent barrier between cells and tissues that prevents functional remodeling of extracellular matrix (ECM). Such nonphysiological membranes hinder transmembrane cross-talk between cells and the study of basement membranes in health and disease. Moreover, PDMS/PC membranes have flat surfaces that lack the topographical features and microstructures found in native tissues that are important for cell fate determination and tissue function (26). An alternative membrane that enables in vivo-like transmembrane intercellular cross-talk and basement membrane remodeling by surrounding cells is needed to enhance the physiological relevance of OOCs.

To address this unmet need, we used silk fibroin (SF) to engineer an alternative class of basement membranes for OOC devices. SF is a protein generated by *Bombyx mori* silkworms that has superior mechanical properties, biocompatibility, and versatility and has been used to create various synthetic materials for drug delivery (27–30), biosensor and bioelectronics (31–33), and tissue engineering (34–36). When SF is exposed to methanol, it undergoes a conformational

¹Department of Biomedical Engineering, Pratt School of Engineering, Duke University, Durham, NC 27710, USA. ²Center for Biomolecular and Tissue Engineering, Duke University, Durham, NC 27710, USA. ³Division of Nephrology, Department of Medicine, Duke University School of Medicine, Durham, NC 27710, USA. ⁴Department of Cell Biology, Duke University, Durham, NC 27710, USA. ⁵Affiliate Faculty of the Developmental and Stem Cell Biology Program, Duke Regeneration Center, Duke MEDx Initiative, Duke University, Durham, NC 27710, USA.

*Corresponding author. Email: samira.musah@duke.edu

†Present address: Harvard-MIT Division of Health Sciences and Technology, Institute for Medical Engineering and Science, Massachusetts Institute of Technology, Cambridge, MA 02139, USA.

transition from random coil to tightly packed β sheet that enhances the mechanical properties of SF-based materials and makes them insoluble in water. SF material properties surpass those of other protein-based biomaterials such as collagen and fibril materials (34), which tend to be more susceptible to rupture under fluid shear stress and handling, making SF a promising candidate for tissue engineering applications. We and others have engineered SF scaffolds that support the propagation and differentiation of various cell types including fibroblasts (37), neurons (38), cardiomyocytes (39), lung epithelial stem cells (40), and kidney cells (41). For example, Sun *et al.* (42) developed an SF film that supports the adhesion and proliferation of skin fibroblasts in a rat wound healing model. Li *et al.* (38) used electrospun SF, which contains nonwoven nanofibers that provide ECM-like topographical structures, to support the proliferation of neural progenitor cells and their differentiation into neurons. Our group demonstrated that electrospun SF membranes enhanced the adhesion and differentiation of human-induced pluripotent stem (hiPS) cell-derived cells when compared to tissue culture plates (41).

Here, we engineered a kidney glomerulus-on-a-chip system by using electrospun SF to create an ultrathin membrane that resembles *in vivo* basement membranes with ECM-like topography and molecular properties and that robustly supports kidney cell propagation, transmembrane intercellular cross-talk, basement membrane remodeling, molecular size-specific glomerular filtration, and an OOC platform capable of inducing the development of fenestrated endothelium from unspecialized hiPS cell derivatives with specificity.

RESULTS

Engineering and characterization of the kidney glomerulus-on-a-chip device

The biomimetic microfluidic (bioMF) OOC device manufacturing process is illustrated in Fig. 1A. SF membranes were generated by electrospinning as described in the Materials and Methods and were sectioned into 5 cm by 0.5 cm rectangles, followed by immersion in 90% methanol for 20 min to induce the conformational change of SF chains from random coils to β sheets. Polyethylene oxide (PEO) was added during electrospinning to increase the solution's viscosity and was removed by immersing the SF membranes in deionized (DI) water for 48 hours. The PEO-free SF membrane was air-dried and attached to a PDMS chip that contained a microfluidic channel (1 mm by 0.2 mm by 18 mm, bottom channel in Fig. 1B) representing the dedicated vascular compartment using spin-coated PDMS glue. The resulting hybrid SF/PDMS chip was then stamped against a second PDMS chip that contained a larger channel (1 mm by 1 mm by 18 mm, top channel in Fig. 1B) representing the urinary filtrate compartment. PDMS glue was used to secure the portions of SF membranes outside the parallel fluidic channels and between the chip walls. The stamping step was performed twice to ensure sufficient spreading and infiltration of the PDMS glue into the SF membranes. The glue was cured at room temperature for 48 hours, and the SF/PDMS bottom chip and a new PDMS top chip were treated with oxygen plasma to facilitate PDMS-PDMS bonding through Si—O—Si covalent bonds. The oxygen plasma treatment also introduced hydroxyl groups on the SF membrane, which increased its hydrophilicity and enhanced adsorption of laminin-511, an ECM protein essential for cell adhesion, propagation, and differentiation (41). To demonstrate the biological function of the chips, we used hiPS cell-derived

vascular endothelial cells and podocytes to reconstitute the structure and function of the human kidney's blood filtration barrier—the glomerular capillary wall—which has a unique three-layered tissue-tissue interface that provides size-selective blood filtration.

The resulting chips contained two fluidic channels separated by a SF membrane (Fig. 1B). Notably, the membrane is an order of magnitude thinner than the PDMS membranes used previously in other OOC devices (21, 22) (3.5 μm versus 45 μm) (Fig. 1, C and D). The SF membranes were highly porous (Fig. 1, E and F), an important feature for molecular transport and intercellular cross-talk between cell layers on opposite sides of the membrane. Despite the desirably high porosity of the SF membrane, the bioMF OOC device did not leak even after prolonged continuous perfusion. The SF membranes also exhibited a microstructure characterized by intertwining layers of fibers resembling the ultrastructure of native ECM (Fig. 1F and fig. S1A). When functionalized with laminin to enhance cell adhesion, the SF membranes retain their characteristic fibrous morphological features, while the individual nanofibers appeared to exhibit a slightly rougher surface topology compared to uncoated membranes, indicating robust incorporation of laminin-511 on the electrospun SF nanofibers (fig. S1A). By contrast, laminin functionalization on porous PDMS membranes resulted in a smoother surface than bare PDMS membranes, where ridges were observed on the surface; however, these ridges can no longer be observed after laminin functionalization (fig. S1B). In addition, the SF membrane had a bulk Young's modulus of ~ 67 kPa (fig. S2A) that is closely related to the mechanical properties of the human kidneys as reported previously (43); this *in vivo*-like topography and mechanical property of electrospun SF can enhance cell propagation and differentiation (44–46).

Naturally derived matrices have batch-to-batch variations in their molecular content (47–49) which limits reproducibility between experiments. To examine whether our engineered platform can avoid this issue, we performed Fourier transform infrared (FTIR) spectroscopy analysis to examine the chemical and functional group characteristics of independently synthesized SF membranes. We found that membranes from different batches exhibited similar infrared absorbance peak patterns, indicating consistent molecular and conformational composition (fig. S2B).

Engineering the glomerular filtration barrier from patient-specific hiPS cells

The glomerulus chip consists of two parallel microfluidic channels, making it amenable to modeling multicomponent tissue systems such as the three-layered podocyte–glomerular basement membrane–endothelial cell interface at the kidney's blood filtration barrier. In our kidney glomerulus-on-a-chip device, the top channel (1 mm by 1 mm cross section) represented the urinary compartment, while the bottom channel (1 mm by 0.2 mm cross section) represented the vascular compartment (schematic in Fig. 1B). To mimic the development of human glomerulus tissue *in situ* (in the engineered device), we differentiated podocytes from hiPS cell-derived intermediate mesoderm cells (IM cells; precursor of podocytes) and cocultured them with vascular endothelial cells derived from the same (isogenic) hiPS cells. The IM cells seeded in the top channel were differentiated into mature podocytes by using media supplemented with defined inductive factors (8), while the cells were interfaced with endothelial cells layered on the opposite side of the SF membrane in the vascular channel. After differentiation, the podocytes formed a uniform cell layer and expressed mature podocyte

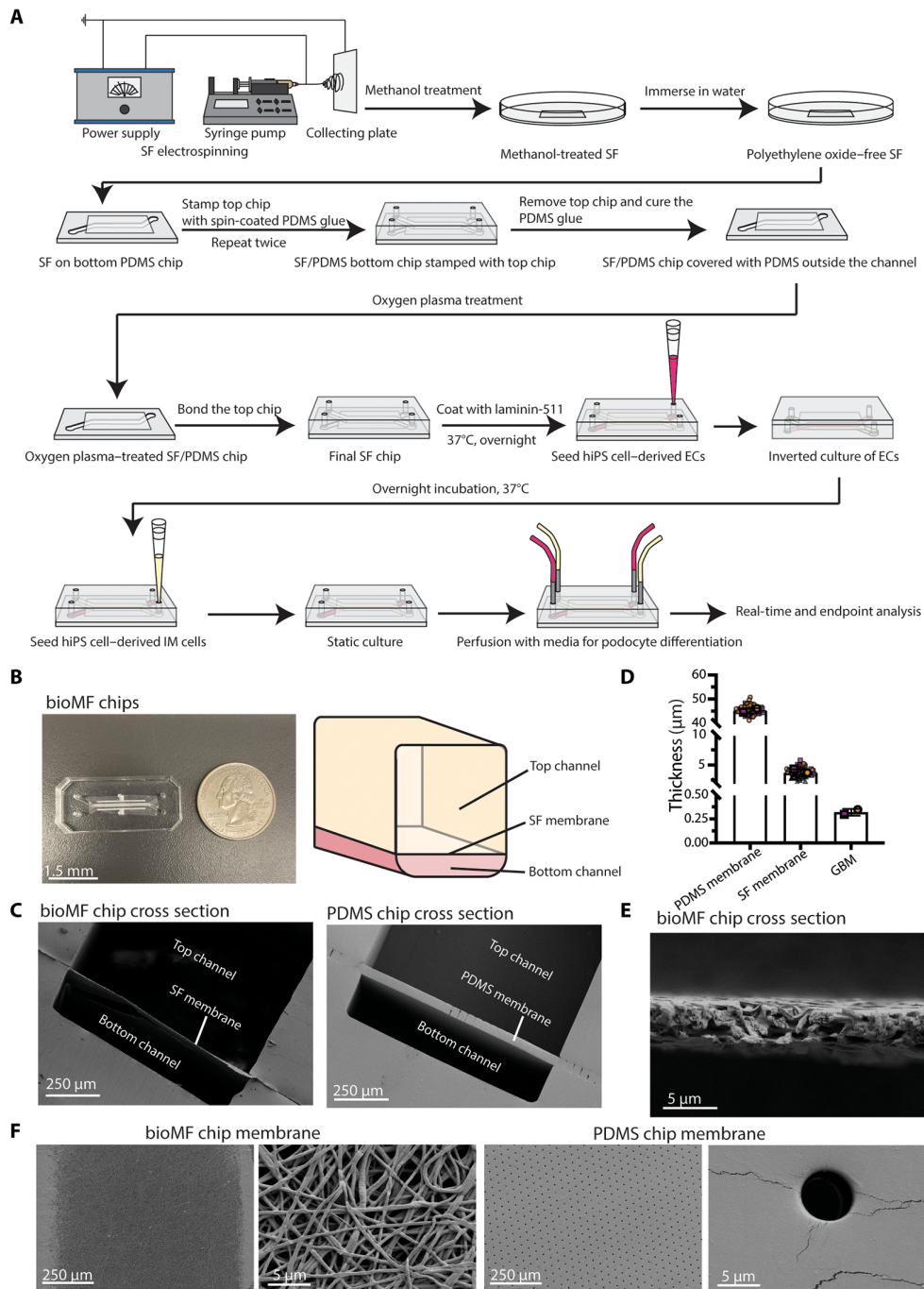


Fig. 1. Glomerulus bioMF device engineering and characterization. (A) Schematic showing SF membrane synthesis and bioMF OOC device manufacturing process. The order of cell seeding and differentiation of hiPS cell-derived podocytes and vascular endothelial cells are illustrated. ECs, endothelial cells; IM, intermediate mesoderm. (B) A representative photograph of the chips (left) and a schematic demonstrating the cross section of the chip (right). Scale bar, 1.5 mm. (C) Electron micrographs showing cross-sectional views of the bioMF OOC device with ultrathin SF membrane (left) and a conventional chip with a substantially thicker PDMS membrane (right). Scale bars, 250 μm. (D) Electron micrograph quantification of membrane thickness in the bioMF OOC device compared to conventional PDMS chips and the estimated in vivo glomerular basement membrane (GBM) thickness (80), $N = 2$ samples for conventional PDMS chips, $N = 3$ samples for bioMF OOC devices, $n = 25$ measurements for each sample. Purple squares (small): individual chip data points from the first replicate; purple squares (large): mean of all chip data points from the first replicate; orange circles (small): individual chip data points from the second replicate; orange circles (large): mean of all chip data points from the second replicate; cyan triangles (small): individual chip data points from the third replicate; cyan triangle (large): mean of all chip data points from the third replicate; (E) zoomed-in view of SF membrane cross section. Scale bar, 5 μm. (F) Electron micrographs showing the morphology, fiber network, and porosity of the SF membrane and a PDMS membrane. Scale bars, 250 μm (the first and the third) and 5 μm (the second and the fourth).

lineage markers, including nephrin and podocin (Fig. 2A), which are important for regulating the formation of podocyte foot processes and blood filtration function (50). Nephrin at the interface between two or more podocyte foot processes maintains the structural integrity of the slit diaphragm, and podocin regulates foot process formation (51, 52). Podocytes differentiated in the chips expressed high levels of nephrin in the resulting tissue areas or boundaries where multiple podocytes interact to form the zipper-like structures or interdigitating foot process-like patterns observed in native tissues. These cellular phenotypes suggest that the podocytes differentiated in situ were mature and formed cell-cell interactions necessary for tissue function (Fig. 2A, top left, middle left, bottom left, and bottom middle images). In addition, podocin formed filamentous distribution patterns in podocytes differentiated in the chips, indicating maturation of the cells and formation of foot processes (Fig. 2A, top right, middle right, and bottom right images). hiPS cell-derived endothelial cells maintained a confluent layer on the opposite side of the SF membrane and expressed the endothelial cell marker vascular endothelial (VE)-cadherin (Fig. 2B), an adhesion molecule essential for regulating cell-cell contact, cell proliferation, and vascular permeability (53). In addition, we found that the endothelial cells lined all sides of the vascular channel (fig. S3, A and B). Given this study's goal of modeling the glomerular filtration barrier, we specifically focused on the endothelial cells lining the SF membrane and at the podocyte-endothelium interface. These analyses revealed the formation of continuous podocyte and endothelial cell layers on the dedicated apical and basal sides of the SF membrane embedded in the microfluidic chip, as confirmed by three-dimensional (3D) confocal imaging of the device (Fig. 2C and fig. S4A). In addition, Western blot analysis further confirmed the presence of mature podocytes and endothelial cells in the bioMF OOC device through the presence of strong bands corresponding to synaptopodin and VE-cadherin (fig. S4B). Synaptopodin is one of the key podocyte markers that binds to the podocyte actin-cytoskeleton, regulating podocyte actin integrity and exerting a protective effect against podocyte injury caused by marked actin cytoskeletal rearrangement or disruption (54).

Podocytes are the major contributors of basement membrane proteins in the native glomerulus (8). We examined ECM protein expression in the glomerular tissue formed in the chips and found that the podocyte layer produced notably more collagen IV than the endothelial cell layer (Fig. 2D and fig. S5), consistent with the mature kidney phenotype. Other key glomerular basement membrane molecules including nidogen-1 and agrin were also secreted by the podocytes and deposited onto the underlying SF membrane, with low to no expression in the endothelial cells (Fig. 2D and fig. S5). Nidogen-1 binds laminin and collagen to facilitate basement membrane formation (55), and agrin is a negatively charged heparan sulfate proteoglycan contributing to the net negative charge of the glomerular basement membrane in vivo. This net negative charge may help restrict filtration and loss of plasma albumin (55). These cell-secreted ECM molecules were deposited onto the underlying SF membrane, suggesting that the SF membrane can be remodeled by podocytes through secretion of glomerular basement membrane molecules to generate a native ECM-like interface between podocytes and endothelial cells.

The kidney's glomerular filtration barrier removes waste from blood by filtering based on molecular size and charge. Large, negatively charged plasma proteins are retained, while smaller waste molecules pass through and enter the urine if they are not reabsorbed. For

example, inulin is a small polysaccharide (3 to 5 kDa) that efficiently crosses the glomerular filtration barrier and is widely used for clinical measurement of glomerular filtration rate in patients (56). In contrast, albumin is a large (66.5 kDa) negatively charged protein that cannot cross the filtration barrier in a healthy kidney and is retained in the vasculature. To determine whether our podocyte- and endothelial cell-lined chip could selectively retain albumin in the vasculature channel while removing inulin by filtration into the urinary filtrate channel, we performed a permselective filtration assay using inulin conjugated to fluorescein isothiocyanate (inulin-FITC) and albumin conjugated to Texas Red (albumin-Texas Red). We found that chips lined with podocytes and endothelial cells showed physiologically relevant levels of selective molecular filtration, removing more than 7% of inulin within 6 hours while retaining more than 99.5% of albumin (Fig. 2E). This selective filtration performance is comparable to estimated in vivo values of 6.6% inulin removal and 99.9% albumin retention in 6 hours (Fig. 2F) (8, 57, 58). The in vivo-like three-component system was essential for achieving selective filtration rates similar to in vivo glomerular filtration rates as chips lacking the specialized glomerular epithelial and endothelial cells failed to prevent the loss of albumin into the urinary outflow (Fig. 2G). These results demonstrate the functionality of the engineered device, enabled by the concerted actions of the two cell layers—podocytes and endothelium—separated by a thin, porous, cell-modified SF membrane.

Urea is another important molecule in glomerular filtration but is often neglected in glomerulus-on-a-chip models. Urea is a small molecule (60 Da) formed by catabolism of the toxic cell metabolic waste molecule ammonia in the liver (59). In the kidneys, urea crosses the glomerular filtration barrier and is excreted with urine. We evaluated urea filtration in our bioMF OOC device and found that urea exhibited higher clearance than inulin and albumin: urea (60 Da), 11% clearance; inulin (3 to 5 kDa), 7% clearance; albumin (66.5 kDa), 0.5% clearance (Fig. 2H). These results demonstrated the size-selective filtration function of the device. In patients with chronic kidney disease, filtration of urea is compromised leading to uremia, a fatal disease if left untreated (60). Dialysis is used to facilitate urea removal for patients with late-stage chronic kidney disease. Two metrics have been used to evaluate the efficiency of urea removal in dialysis, Kt/V (K : dialyzer clearance; t : dialysis time; V : urea distribution volume) and URR (urea reduction ratio), with the National Kidney Foundation's dialysis guidelines (61) recommending a Kt/V of ≥ 1.2 and URR of $\geq 65\%$. In our device, Kt/V reached 1.8 and URR was 83% (table S1), surpassing the recommended values, indicating that the bioMF OOC device can remove urea and meet dialysis standards. As a result, we anticipate that the device can be further explored as a potential blood filtration device for removal of urea and other uremic toxins in future work. Together, these selective molecular filtration results demonstrate that the bioMF OOC device exhibits size-selective molecular filtration resembling the human kidney glomerulus.

Glomerular disease modeling

Glomerular diseases are associated with various risk factors including drug toxicity (62), genetics (63), bacterial and viral infections (64, 65), and patient lifestyle (66). Recapitulation of glomerular injury phenotypes in a bioMF chip would provide a valuable platform for drug discovery and mechanistic studies. We tested whether the glomerulus chips could recapitulate nephrotoxicity by administering the chemotherapy drug Adriamycin (ADR), which causes acute

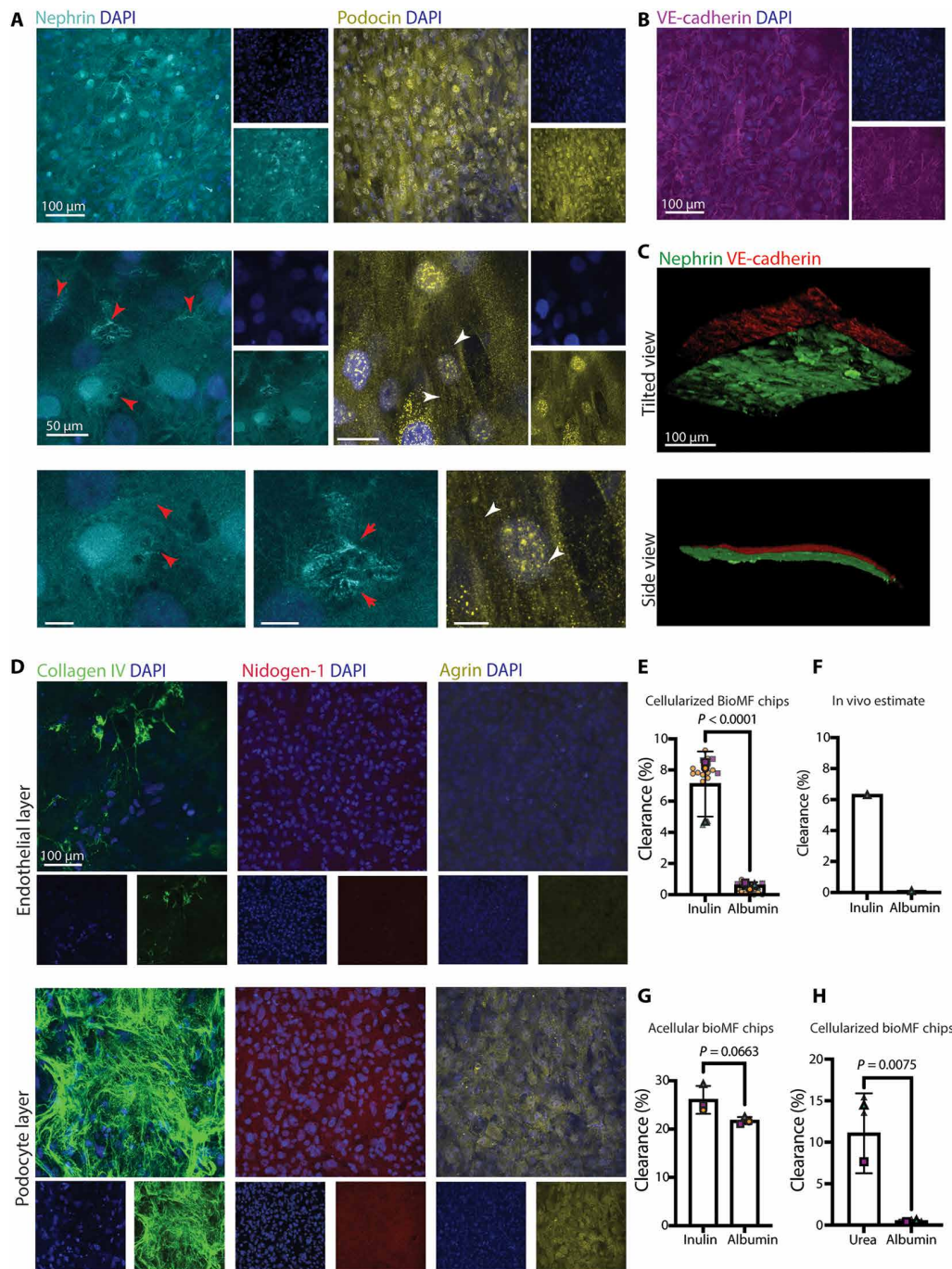


Fig. 2. Enhanced cell differentiation and glomerular tissue formation in the bioMF OOC device. (A) Confocal microscopy of hiPS cell–derived podocytes differentiated in the device and immunostained for cell lineage identification markers nephrin (cyan) and podocin (yellow) and counterstained with 4',6-diamidino-2-phenylindole (DAPI; blue). Red arrows indicate strong expression of nephrin at the cell boundaries, and white arrows indicate filamentous pattern of podocin in podocytes. Scale bars: 100 μm (top row), 50 μm (middle row), and 25 μm (bottom row). (B) Confocal microscopy of the hiPS cell–derived endothelial cells cultured in the device and immunostained for the endothelial marker VE-cadherin (magenta) and counterstained with DAPI (blue). Scale bar, 100 μm . (C) 3D reconstructed images of the epithelial (podocyte) and vascular (endothelial) cell layers separated by the electrospun SF membrane in the device. Cells were immunostained for nephrin (green) and VE-cadherin (red). Scale bar, 25 μm . (D) Characterization of cell-secreted basement membrane proteins in the chips. Cultured glomerulus bioMF devices were immunostained for the ECM proteins collagen IV (first column, green), nidogen-1 (second column, red), and agrin (third column, yellow). Scale bar, 100 μm . (E) Inulin and albumin filtration function of the cellularized devices with podocytes and endothelial cells; $N = 3$ independent replicates. (F) Estimated inulin and albumin filtration rate in vivo (8). (G) Inulin and albumin filtration function of acellular devices; $N = 3$ independent replicates. (H) Urea and albumin filtration function of the cellularized devices with podocytes and endothelial cells, $N = 2$ independent replicates. Cyan triangles (small): chip data points from the first replicate; cyan triangle (large): mean of all first replicate chip data points; orange circles (small): chip data points from the second replicate; orange circles (large): mean of all second replicate chip data points; purple squares (small): chip data points from the third replicate; purple squares (large): mean of all third replicate chip data points. Statistical analysis was performed using unpaired Student's t test.

glomerular injury in patients (67, 68), to the vascular channel of the device to mimic intravenous drug administration. After 3 days of exposure to a clinically relevant dose of ADR (0.5 $\mu\text{g}/\text{ml}$), the glomerulus bioMF OOC devices developed compromised cellular phenotypes and aberrant filtration function. Podocytes in the ADR-treated chips lost foot processes, became less arborized than the vehicle control [dimethyl sulfoxide (DMSO)-treated chips], and exhibited obscure cell-cell boundaries (Fig. 3A), characteristics of injured kidney glomeruli. These observations were supported by the altered expression pattern of podocin; filamentous podocin distribution patterns were no longer observed in the ADR-treated chip's podocyte layer, where podocyte loss was apparent (Fig. 3, A and B). These observations are consistent with previous studies that showed podocyte foot process effacement due to ADR-induced podocyte injury (8, 69). In contrast, the endothelial cells maintained their structure and VE-cadherin expression after ADR treatment (Fig. 3C), successfully modeling cell type-specific sensitivity to ADR observed in the kidney glomerulus (70, 71).

Permeable molecular filtration was also compromised upon ADR treatment of the chip. Both inulin and albumin clearance rates were significantly higher in the ADR-treated group than in the DMSO-treated control (Fig. 3, D and E), indicating the onset of albuminuria and loss of size-selective filtration upon exposure to the drug. These results mimic clinical indicators of microalbuminuria in acute kidney injury, in which elevated albumin in patient urine is observed (70).

The demonstration of drug-induced nephrotoxicity in the chips indicates their ability to recapitulate pathophysiological outcomes in response to injury stimuli. Thus, the glomerulus chip platform can be useful for screening drugs for nephrotoxicity, studying disease mechanisms and discovering new therapeutic candidates.

Induction of fenestrated glomerular endothelium from hiPS cells

OOCs are often challenging to section for high-resolution electron microscopy due to material mechanical property mismatch between the elastic PDMS and rigid cured resins used for tissue embedding and processing. The ultrathin SF membrane-containing chips developed in this study allow easy microtome sectioning for applications in high-power tissue characterization and analysis of cell morphological features (Fig. 4A).

High-resolution transmission electron microscopy (TEM) analysis confirmed that the podocytes and endothelial cells propagated in the glomerulus chips formed respective tissue layers on opposite sides of the SF membrane, creating a sandwich-like three-layered tissue structure that mimics the *in vivo* glomerular filtration barrier (Fig. 4B). In the glomerulus chips, podocytes formed long protrusions (foot processes; indicated by red arrows in the left image in Fig. 4C). Intriguingly, some of the podocyte foot processes encased the engineered SF membrane and wrapped around individual electrospun SF nanofibers, forming secondary and tertiary foot processes (green arrows in the middle image in Fig. 4C), indicating robust cell attachment and interaction with the SF membrane (orange arrows in the right image in Fig. 4C). The formation of primary, secondary, and tertiary foot processes indicates a mature podocyte phenotype capable of forming interdigitations with neighboring cell's foot processes to facilitate glomerular filtration (72). The SF membranes exhibit high porosity (55.9% void/pore area in the SF membrane cross section; fig. S6) with interconnected pores amenable to

diffusion and transport of nutrients and signaling molecules across the engineered glomerular filtration barrier. Despite the high porosity, both podocytes and endothelial cells remained adherent to their respective sides of the SF membrane surfaces, without undesirable infiltration into the adjacent tissue. This observation accurately recapitulates the structural organization and features of the healthy glomerular filtration barrier *in vivo*, where podocytes and endothelial cells are proximal to each other but remain on either side or surface of the ultrathin glomerular basement membrane (73). The thinness of the SF membrane positions podocytes and endothelial cells proximally, enabling intercellular cross-talk and formation of *in vivo*-like tissue-tissue interfaces. We found that hiPS cell-derived endothelial cells developed fenestrations only when interfaced with podocytes in the chip (Fig. 4, B to D); ~40% of the endothelial cell body constituted the characteristic void-like fenestration morphology (fig. S7). Endothelial cells propagated without podocytes in the chip failed to form the highly specialized fenestration-like structures observed *in vivo* (Fig. 4E and fig. S7). By quantifying the number of fenestrations per pixel in the differentiated endothelial cells, we found that the number of fenestration-like structures was significantly higher when endothelial cells were cocultured with podocytes than when podocytes were absent (Fig. 4F). To visually highlight the distinct cell layers and resulting tissues formed on the SF membrane, we generated pseudo-colored versions of the TEM micrographs shown in Fig. 4 (B and E, middle) (Fig. 4, G and H). These pseudo-colored images reveal the formation of fenestrations by endothelial cells interfaced with podocytes in the chip.

Fenestrations are a key morphological feature of the glomerular endothelium and are induced *in vivo* by endothelial cell interactions with podocyte-secreted vascular endothelial growth factor A (VEGF-A) via the VEGF receptor 2 (VEGFR2) (74). Subsequent activation of phosphatidylinositol 3-kinase signaling and rearrangement of the endothelial cell cytoskeleton enable fenestrae development (74). Intriguingly, methods to induce this tissue-specific endothelial phenotype *in vitro* from differentiated hiPS cells have yet to be explored (75). The ability to generate this specialized cell type in this study suggests that the proximity of the podocytes and endothelial cells in the chip supported robust intercellular communication that allowed formation of a tissue-tissue interface and tissue-specific morphogenesis. To explore whether VEGF-A signaling between podocytes and endothelial cells occurs in the chips, we examined the expression of VEGF-A in both podocytes and endothelial cells in the devices (Fig. 5, A and B). We observed VEGF-A expression in the podocytes when cocultured with endothelial cells (Fig. 5B and fig. S8), but when only podocytes or only endothelial cells were cultured in the device, the cells failed to form a confluent monolayer and podocyte expression of VEGF-A was low or near background levels (Fig. 5B and fig. S8). These results indicate that coculturing podocytes and endothelial cells in the chips leads to the development of a specialized cell phenotype and that interactions between the podocyte and endothelial tissue layers across the ultrathin SF membrane facilitates podocyte maturation and production of VEGF-A to promote glomerular endothelial cell specialization. We quantified intracellular expression of VEGF-A and its secretion by cells into the soluble medium in the chips. A VEGF-A concentration of ~14 ng/ml was found in the top channel (Fig. 5C), indicating secretion of VEGF-A from podocytes. Meanwhile, despite the drastically low levels of intracellular VEGF-A expression in the endothelial cell layer (Fig. 5B), a VEGF-A concentration of approximately 2.5 ng/ml was detected in

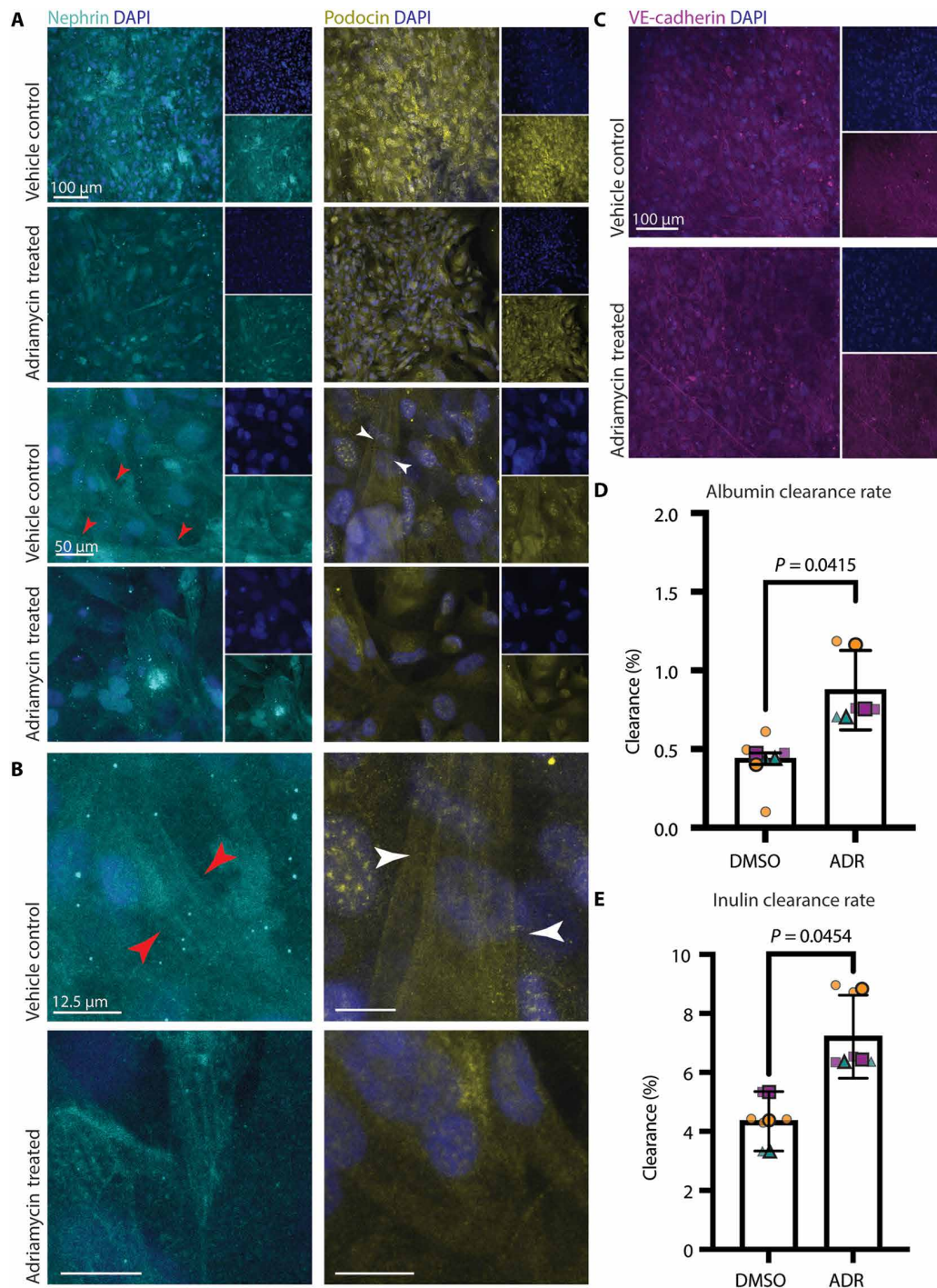


Fig. 3. Modeling drug-induced nephrotoxicity in the glomerulus-on-a-chip. (A) Fluorescent images of podocytes in the devices with and without ADR treatment, immunostained for nephrin (cyan) and podocin (yellow) and counterstained with DAPI (blue). Red arrows indicate strong expression of nephrin on the cell boundaries, and white arrows indicate filamentous pattern of podocin in podocytes. Scale bars, 100 μm (top two rows) and 25 μm (bottom two rows). (B) Digital zoom-in of the podocyte fluorescent images from (A), immunostained for nephrin (cyan) and podocin (yellow) and counterstained with DAPI (blue). Red arrows indicate strong expression of nephrin at the cell boundaries, and white arrows indicate filamentous pattern of podocin in podocytes. Scale bars, 12.5 μm . (C) Fluorescent images of the endothelial cells in the devices with and without ADR treatment, immunostained for VE-cadherin (magenta) and counterstained with DAPI (blue). Scale bar, 100 μm . (D) Albumin filtration function of nontreated (vehicle control) and ADR-treated OOC devices; $N = 3$ independent replicates. (E) Inulin filtration function of vehicle control and ADR-treated devices; $N = 3$ independent replicates. Cyan triangles (small): individual chip data points from the first replicate; cyan triangle (large): mean of all chip data points from the first replicate; orange circles (small): individual chip data points from the second replicate; orange circles (large): mean of all chip data points from the second replicate; purple squares (small): individual chip data points from the third replicate; purple squares (large): mean of all chip data points from the third replicate. Statistical analysis was performed using unpaired Student's *t* test.

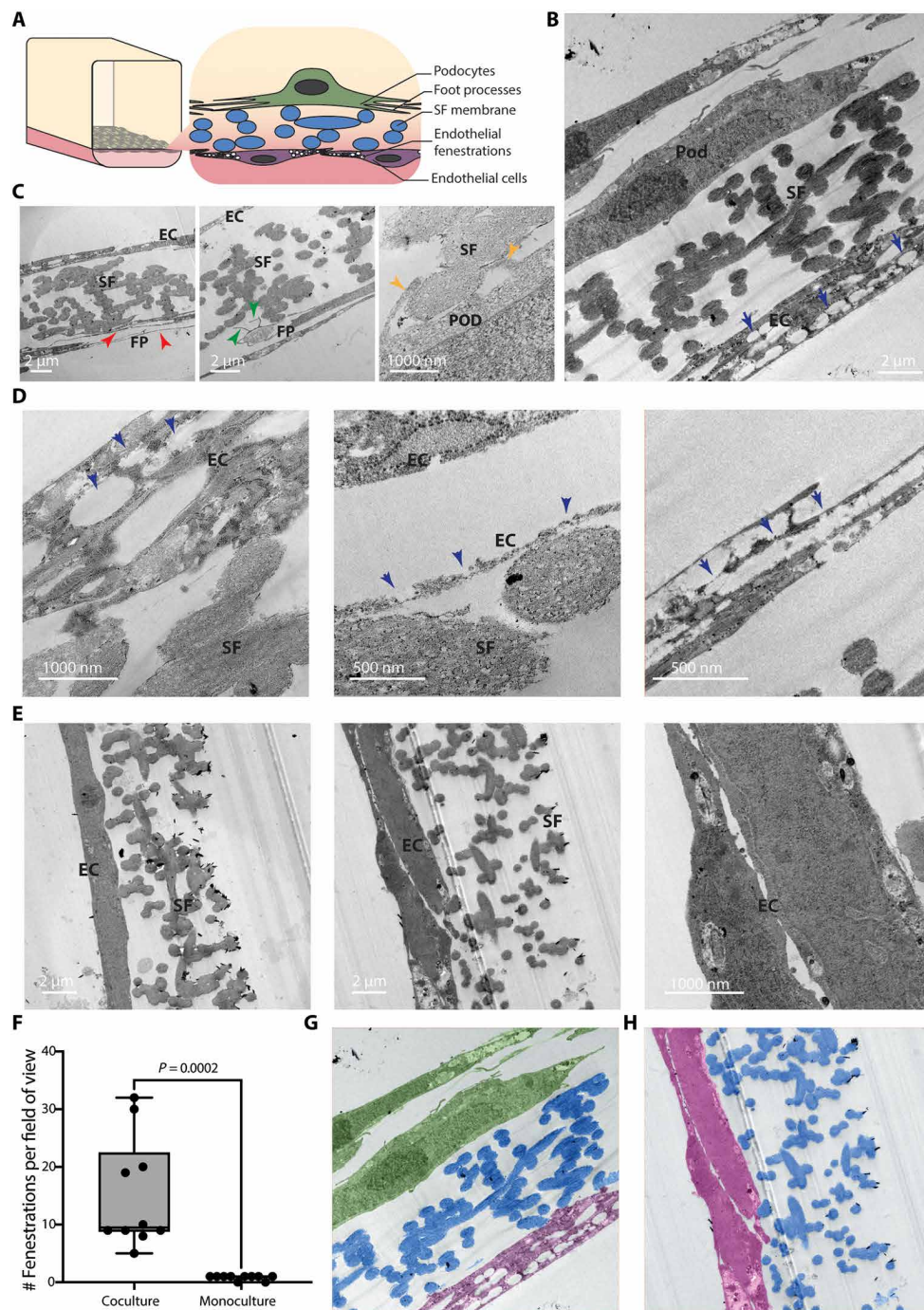


Fig. 4. High-resolution electron microscopy analysis of tissue-specific phenotypes in the engineered glomerulus bioMF device. (A) Schematic highlighting the cross-sectional view of the engineered tissue model and structure. (B) Transmission electron micrograph showing an actual cross-sectional view of the engineered glomerular filtration barrier in the chips. Scale bar, 2 μm . (C) TEM images of podocytes and endothelial cells in the chips. Red arrows indicate podocyte foot processes and formation of interdigitated-like organization, green arrows indicate formation of secondary and tertiary foot processes, and orange arrows indicate formation of short protrusions around the SF nanofibers. Scale bars, 2 μm (left and middle) and 1 μm (right). EC, endothelial cells; SF, SF membrane; POD, podocytes; FP, foot processes. (D) TEM images of endothelial cells phenotype in the chips when interfaced with podocytes. Blue arrows indicate fenestration-like structures. Scale bars: 1000 nm (left), 500 nm (middle), and 1 μm (right). (E) TEM images of endothelial cells in the chips when podocytes were absent. Scale bars, 2 μm (left and middle) and 1000 nm (right). (F) Quantification of endothelial cell fenestration numbers in regions of interest from TEM images in coculture/monoculture chips. $N = 10$ field of views on different cells. (G) Pseudo-colored electron micrograph of podocytes (green) and fenestrated endothelial cells (purple) in the chips showing each cell layer on opposing sides of the SF membrane (blue), demonstrating the engineered model of the glomerular filtration barrier. (H) Pseudo-colored electron micrograph of monolayer-cultured endothelial cells (purple) in the chips on the SF membrane (blue), underscoring the lack of fenestrae when podocyte interactions are absent. Statistical analysis was performed using unpaired Student's *t* test.

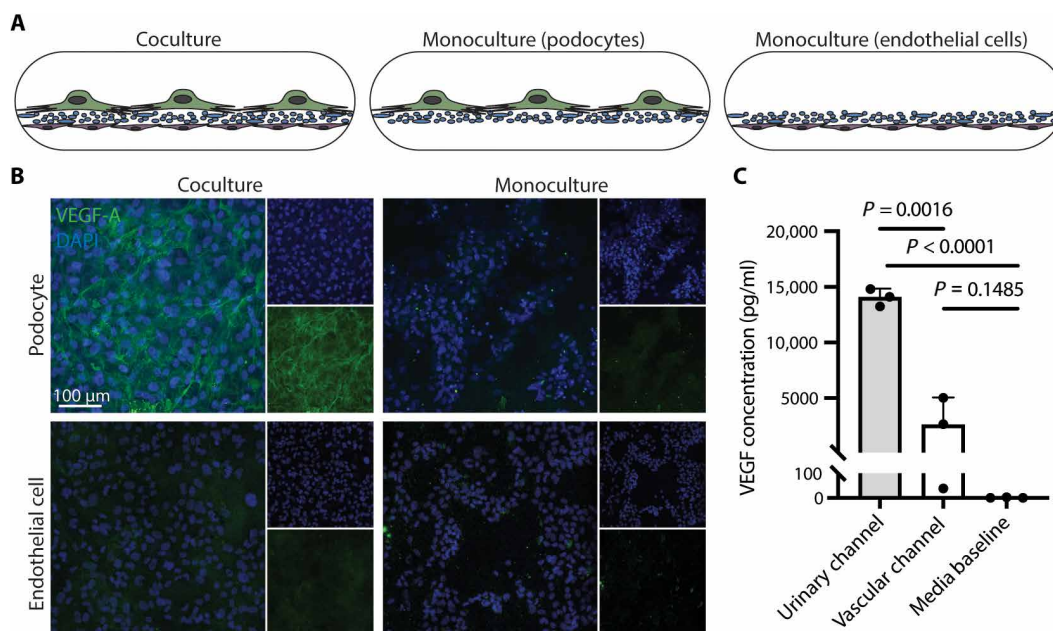


Fig. 5. Uncovering intercellular cross-talk in the engineered glomerulus-on-a-chip. (A) Schematic showing cell culture conditions in the chips. Left: Podocytes and endothelial cells are cocultured in the chip. Middle: Only podocytes are cultured in the chip. Right: Only endothelial cells are cultured in the chip. (B) Confocal microscopy images evaluating VEGF-A expression in the podocyte and endothelial cell layers under coculture and monoculture conditions in the devices. Scale bar, 100 μm. (C) ELISA characterization of secreted VEGF-A concentration in the urinary and vascular channels in the cocultured chips; $N = 3$ independent samples. Statistical analysis was performed using unpaired Student's *t* test.

the vascular channel fluid outflow (Fig. 5C). In contrast, there were undetectable levels of VEGF-A in the cell culture medium alone (background or medium unexposed to the cells) (Fig. 5C). Together, these data underscore the functional characteristics of the bioMF OOC device, which include podocyte production and secretion of VEGF-A. The presence of soluble VEGF-A in the vascular channel along with the formation of fenestration in the endothelial cells indicated that the chips supported VEGF-A production by the podocytes and cross-talk between podocytes and endothelial cells to induce a specialized glomerular endothelial phenotype from a generic vascular endothelial cell population derived from undifferentiated hiPS cells. Thus, this bioMF OOC system could be used to study intercellular signaling across basement membranes in the kidney glomerular filtration barrier and in other organ models.

DISCUSSION

In this study, we engineered a type of OOC device by integrating an ultrathin electrospun SF biomimetic basement membrane to interface two tissue layers (glomerular epithelium and vascular endothelium) in a dynamic microfluidic system. The resulting device supports the differentiation and propagation of hiPS cell-derived kidney glomerular cells, podocytes, and vascular endothelial cells, to generate an isogenic human glomerulus-on-a-chip that exhibits *in vivo*-like cell structure, tissue organization, ECM remodeling, and molecular filtration functions. Intriguingly, we observed that the SF membranes support cyclic mechanical stretching (movie S1), suggesting that the SF membranes would be amenable to physiological levels of mechanical strain, which could be a topic for follow-up studies, especially when applying this new organ-on-a-chip system to model lung function or

inter-organ communication and cross-talk in the future. We also demonstrated the utility of the device for modeling glomerular injury and proteinuria disease. The porous structure of the electrospun SF membrane supported the integration of basement membrane proteins secreted by the surrounding podocytes and endothelial cells, yielding a physiologically relevant scaffold for prolonged tissue culture, differentiation, and maturation. The ultrathin (3.5-μm thick) membrane was amenable to microtome sectioning of the bioMF OOC devices for high-resolution TEM analysis, which has been challenging to perform using PDMS membrane-based OOC devices, as microtome blades cannot easily cut through the thick, elastic PDMS membranes embedded in resins. TEM analysis revealed that the glomerulus bioMF device supports formation of a tissue-tissue interface when podocytes and endothelial cells are cocultured on opposing side of the SF membrane, in which unspecialized vascular endothelial cells develop fenestrations that mimic the unique morphological and functional feature of glomerular endothelial cells *in vivo*.

Future studies could use this platform to gain insight into the mechanisms of fenestrae development and cell fate determination, including the roles of intracellular vesicles and their aggregation and fusion to form openings in the cell cytoplasm (74) by examining endothelial morphology at different time points in the bioMF OOC device. The capability to recapitulate *in vivo*-like podocyte-endothelial cross-talk and fenestrae development will help elucidate the mechanism by which disruption of specific signaling pathways alters the function of tissue-specific endothelium and influences disease progression (e.g., drug-induced nephrotoxicity, viral infection, and pathogenic genetic mutations). Because the electrospinning methodology used here can produce membranes of different desired thicknesses, future work could

involve modulation of SF membrane thickness to investigate its impact on cell physiology and tissue-tissue cross-talk and to study the role of basement membrane thickness in kidney disease and organ failure. For example, there might be an optimum SF membrane thickness to achieve *in vivo*-like cellular responses in different tissues and organs. In addition, since glomerular basement membrane thickening is a hallmark of several glomerular disorders [e.g., membranous nephropathy (76), diabetic nephropathy (77), and focal segmental glomerulosclerosis (78)], understanding how membrane thickness affects podocyte-endothelial cell cross-talk could improve the understanding of kidney disease mechanisms and help identify previously unidentified therapeutic targets.

To demonstrate the functional capability of the bioMF OOC device, we focused on recapitulating the glomerular filtration barrier because of its characteristic three-layered structure and blood filtration function, which benefit from the structural organization of the chip and the ultrathin, porous SF membrane. The selective molecular filtration of albumin, inulin, and urea only after incorporating podocytes and endothelial cells in the device (not in acellular chips) indicates that the cell layers regulate the filtration rates of these molecules. This strategy for engineering the bioMF OOC device is broadly applicable to other tissues and organs, including brain, heart, and lung tissues via the propagation, differentiation, and maturation of neurons (38), cardiomyocytes (39), and lung epithelial stem cells (40), respectively. Using the layered chip design and SF membrane, various tissue types can be modeled *in vitro* by incorporating their corresponding cell types and by modulating the thickness of the SF membrane and its functionalization with tissue-specific or cell-adhesive ECM proteins. For example, the chips could be functionalized with user-defined matrices that support the coculture of astrocytes, pericytes, and endothelial cells to recapitulate the structure and function of the blood-brain barrier to model neurological disorders such as stroke. Building on this strategy, it may be possible to create networks of organ-specific chips toward the development of “body-on-a-chip” systems for systemic mechanistic studies of human physiology and pathophysiology and for the discovery and testing of therapeutic candidates.

As demonstrated in this study, electrospun SF membranes provide an ultrathin, porous, biocompatible scaffold alternative to synthetic polymers such as PDMS and PC for OOC engineering. Still, SF membranes have limitations that could be addressed in future studies. For example, the membranes have limited translucence, which prevents visualization of nonfluorescently labeled cells during live culture with standard microscopy. The use of reporter cell lines may be required for experiments that involve extensive live-cell imaging. As a result, the chips are better suited for end-point morphological characterization such as by immunofluorescence, electron microscopy, quantitative polymerase chain reaction (PCR), Western blot, and enzyme-linked immunosorbent assay (ELISA). However, the SF membranes were still sufficiently translucent to allow tracking of cell spreading, and we noticed that when IM cells were not properly attached and spread, they formed clumps, observed as large dark cell clusters under a phase contrast or a dissecting microscope, and when the endothelial cells were not properly attached, they formed thick strings along the chip channel walls (fig. S9). The absence of these cell clusters and strings indicated well-spread cell cultures and formation of intact epithelial and endothelial tissue layers in the bioMF OOC device.

MATERIALS AND METHODS

Generation of electrospun SF membranes

A total of 5% SF aqueous solution (Advanced Biomatrix, 5154) was dialyzed against 90% polyethylene glycol (Sigma-Aldrich, P6667) aqueous solution in a Slide-A-Lyzer Dialysis Cassette (Thermo Fisher Scientific, 66380) for 22 hours at room temperature (34), followed by reconstitution in ultrapure water to achieve an 8% SF solution. The solution was mixed gently with 10% PEO (Sigma-Aldrich, 189456) aqueous solution at a ratio of 3.9:1 SF:PEO and was loaded into a 10-ml syringe (BD Biosciences, 14-823-2A) (slowly to prevent air bubble formation). A 16-gauge blunt-tip needle (McMASTER-CARR, 75165A753) was attached to the syringe, and the syringe was loaded onto a syringe pump (Chemyx, F10071) to provide a flow rate of 0.015 ml/min. For electrospinning, power was provided by a high-voltage power supply (Gamma High Voltage Research, ES100P-20 W) at 11 kV, and the SF:PEO mixture solution was electrospun onto flat nonstick aluminum foil at a distance of 20 cm for 10 min. The resulting electrospun mats were used immediately for device engineering (described below) or stored at 4°C.

BioMF OOC device engineering

PDMS chips were generated by casting a prepolymer mixture containing Sylgard 184 elastomer and curing agent (Ellsworth, 184 SIL ELAST KIT 0.5KG) at a ratio of 10:1 in custom-designed 3D-printed molds, including a top channel mold with a 18 mm by 1 mm by 1 mm (*L* by *W* by *H*) dimension and a bottom channel mold with a 18 mm by 1 mm by 0.2 mm dimension (Protolabs) for 4 hours at 65°C. The resulting PDMS chips were peeled from the molds and stored at room temperature. To assemble the chips, electrospun SF/PEO membranes were cut into 5 cm by 0.5 cm rectangles and immersed in 90% methanol solution for 20 min in a fume hood. Afterward, the membranes were air-dried overnight at room temperature in the fume hood, followed by immersion in DI water for 48 hours to remove the PEO. Subsequently, the membranes were air-dried at room temperature and peeled from the foil. The resulting SF membranes were transferred onto a bottom PDMS chip prestamped with spin-coated PDMS prepolymer mixture glue (3500 rpm for 10 min) that contained Sylgard 184 elastomer and curing agent at a ratio of 10:3. The SF/PDMS bottom chip was stored at room temperature overnight to allow the PDMS glue to cure. A top PDMS chip was then stamped with the spin-coated PDMS glue and stamped against the SF/PDMS bottom chip to coat the area of the SF membrane positioned outside the fluidic microchannel with PDMS glue, followed by curing of the PDMS glue for overnight at room temperature. The SF/PDMS bottom chip was then coated with PDMS glue again using the same method, followed by curing of the PDMS glue for 48 hours at room temperature. Subsequently, a new top PDMS chip and the SF/PDMS bottom chip were treated with oxygen plasma at 50 W and 0.8 mbar for 60 s using a plasma asher (Emitech, K-1050X). The top PDMS chip was pressed against the SF/PDMS bottom chip while carefully aligning the fluidic microchannels. Immediately after bonding the chips, 25 μ l of laminin-511 solution (25 μ g/ml; Biolamina, LN511) was added to the bottom channel of the chip and 30 μ l to the top channel of the chip, followed by incubation at 37°C overnight.

hiPS cell culture

The hiPS cell line PGP-1 (Personal Genome Project) was propagated on six-well tissue culture-treated polystyrene plates (VWR, 10062-892) coated with pluripotent stem cell-qualified Matrigel (BD

Biosciences, 354277). The cells were cultured in mTeSR1 medium (Stem Cell Technologies, 85857) and incubated at 37°C and 5% CO₂, and the medium was replenished daily. The cells were passaged every 4 to 5 days by treatment with StemPro Accutase (Thermo Fisher Scientific, 07920). The cells were tested quarterly for and were found to be free of mycoplasma contamination (Mycoplasma PCR Detection Kit, Applied Biological Materials, G238). Chromosomal analysis confirmed that these cells were karyotypically normal.

Differentiation of IM cells

The hiPS cells were dissociated from Matrigel-coated plates by treatment with enzyme-free cell dissociation buffer (Thermo Fisher Scientific, 13150016) and were centrifuged for 5 min at 200g in Dulbecco's modified Eagle's medium (DMEM)/F12. The cells were resuspended in a mesoderm differentiation medium containing DMEM/F12 with GlutaMAX (Gibco, 10565042) supplemented with activin A (100 ng/ml; Thermo Fisher Scientific, PHC9561), 3 μM CHIR99021 (Stemgent, 04-0004), 10 μM Y27632 (Tocris Bioscience, 1254), and 1× B27 serum-free supplement (Gibco, 17504044). The cells were seeded at a density of 100,000 cells per well of a 12-well tissue culture-treated polystyrene plates (VWR, 10062-894) coated with laminin-511-E8 (5 μg/ml; iMatrix-511, T304) solution in sterile distilled water (Gibco, 15230204). The cells were then cultured for 2 days with mesoderm differentiation media at 37°C and 5% CO₂, and the culture medium was replaced with an intermediate mesoderm induction medium (IM medium) containing DMEM/F12 with GlutaMAX supplemented with BMP7 (100 ng/ml; Thermo Fisher Scientific, PHC9541), 3 M CHIR99021, and 1× B27 serum-free supplement. The cells were incubated at 37°C and 5% CO₂ for a minimum of 14 days with daily medium replacement.

Differentiation of endothelial cells

A previously established protocol was adapted for the differentiation of endothelial cells (10, 79). Briefly, hiPS cells were propagated on six-well tissue culture-treated plates coated with Matrigel and were cultured with mTeSR1 supplemented with 10 μM ROCK inhibitor Y-27632 medium for 1 day at 37°C and 5% CO₂, followed by culturing with N2B27 media (neurobasal media; Invitrogen, 21103049) and DMEM/F12 GlutaMAX (Invitrogen) at a 1:1 ratio with 100× N2 (Invitrogen, 17502048) and B27 (–) vitamin A (Invitrogen, 12587010) supplemented with 8 μM CHIR99021 (Stemgent) and Hbpm4 (25 ng/ml; PeproTech, 120-05ET). The cells were cultured in N2B27 media for 3 days (without media exchange) at 37°C and 5% CO₂ to induce lateral mesoderm differentiation. Afterward, N2B27 media was replaced with endothelial induction media containing StemPro-34 SFM media (Invitrogen, 10639011) supplemented with GlutaMAX and penicillin-streptomycin (Pen/Strep) (Gibco Cell Culture, 15140122) at a 100:1:1 ratio, 2 μM forskolin (Abcam, ab120058), and VEGF (200 ng/ml; Invitrogen, PHC9391). The endothelial induction media was exchanged daily for 2 days, and conditioned media was collected 1 day after each media exchange. The cells were then dissociated with Accutase and magnetic-activated cell sorting (MACS)-sorted using QuadroMACS Separator (Miltenyi Biotec, 130-042-302) to harvest CD144⁺ and CD31⁺ cells using human CD144 microbeads (Miltenyi Biotec, 130-097-857) and human CD31 microbeads (Miltenyi Biotec, 130-091-935). The sorted cells were propagated on a tissue culture-treated plate (six-well polystyrene plates, VWR) coated with human fibronectin (25 μg/ml; Advanced Biomatrix, 5050) and cultured with the conditioned media/StemPro-34 SFM

(1:1) supplemented with heparin (2 μg/ml; STEMCELL Technologies, 7980). Media was exchanged every 2 days until the conditioned media was used up. The cells were further propagated with CultureBoost medium (Cell Systems, 4Z0-500-R) supplemented with Pen/Strep (100 U/ml).

Cell seeding, podocyte differentiation, and cell culture in the bioMF OOC device

Before cell seeding, the chip bottom channels were rinsed with 200 μl of prewarmed CultureBoost medium supplemented with Pen/Strep (100 U/ml), and the chip top channels were rinsed with 200 μl of prewarmed DMEM/F12. The chips were then kept at 37°C until later use. Vascular endothelial cells derived from hiPS cells were dissociated from the six-well plate by incubating them with Accutase (2 ml per well; Invitrogen) for 5 min at 37°C and then transferred to a 15-ml conical tube (VWR, 10026-076). The cell suspension was centrifuged for 5 min at 200g, and the supernatant was aspirated. Then, the cell pellet was resuspended to 6 × 10⁶ cells/ml suspension using prewarmed CultureBoost medium supplemented with Pen/Strep (100 U/ml). For endothelial cell seeding, the chip bottom channel media were removed by using a 200-μl pipette, followed by adding 25 μl of the endothelial cell suspension into the same bottom channel. After adding the cell suspension, the chip was immediately flipped over to allow cell adhesion to the SF membrane. The chips were incubated at 37°C and 5% CO₂ for 4 hours to ensure cell attachment. Then, the chip bottom channels were rinsed again with prewarmed CultureBoost supplemented with Pen/Strep (100 U/ml), and the top channels were rinsed with prewarmed DMEM/F12. The chips were incubated in the upside-down orientation for overnight at 37°C and 5% CO₂.

To prepare for intermediate mesoderm cell seeding, the chip's fluidic channels were gently rinsed with CultureBoost medium supplemented with Pen/Strep (100 U/ml; bottom channel) and IM media supplemented with Pen/Strep (100 U/ml; top channel) and incubated at 37°C and 5% CO₂ while preparing the cell suspension. IM cells in a 12-well plate were dissociated with 0.05% trypsin/EDTA (500 μl per well; Gibco) by incubating for 5 min at 37°C. Then, the cells were further dissociated using a cell scraper (Corning) and collected into 2 ml of trypsin neutralization buffer [10% heat-inactivated fetal bovine serum (HI-FBS), Sigma-Aldrich, in DMEM/F12] for each 500 μl of trypsin/EDTA. The cell suspension was centrifuged for 5 min at 200g, and the supernatant was aspirated. The cells were then resuspended to 200,000 cells/ml concentration using prewarmed IM media supplemented with Pen/Strep (100 U/ml). For seeding the IM cells, the chip top channel medium was removed gently using a 200-μl pipette, followed by adding 30 μl of the IM cell suspension into the same top channel. The chips were then incubated at 37°C and 5% CO₂ for 4 hours before gently rinsing the chip bottom and top channels again with prewarmed CultureBoost and IM media, respectively. Subsequently, both the IM cells and the endothelial cells in the chips were incubated overnight at 37°C and 5% CO₂. Afterward, the chip top channel was rinsed gently with prewarmed podocyte induction media consisting of DMEM/F12 with GlutaMAX supplemented with VEGF (50 ng/ml), 1× B27, activin A (100 ng/ml), BMP-7 (100 ng/ml), 0.1 μM all-trans retinoic acid (STEMCELL Technologies, 72262), and 3 μM CHIR99021 supplemented with Pen/Strep (100 U/ml), and the chip bottom channel was rinsed gently with prewarmed media consisting of CultureBoost supplemented with Pen/Strep (100 U/ml), followed by further incubation overnight at 37°C and 5% CO₂.

Subsequently, the chips were connected to the Human Emulation System (Emulate Inc.) to provide the top and bottom channels with pulsatile flow of the podocyte induction media and the CultureBoost (for endothelial cells) at a flow rate of 1 $\mu\text{l}/\text{min}$. The chips were perfused at the flow rate of 1 $\mu\text{l}/\text{min}$ in a 37°C and 5% CO₂ incubator for 4 days, and the media reservoirs were replenished every 2 days. Results demonstrating Nidogen-1 and Agrin production, as well as VEGF-A immunostaining and secretion, were obtained by perfusing the chips using a different peristaltic pump (Ismatec Ip Digital peristaltic pump, Cole-Parmer, EW-78001-32) at a flow rate of 4.09 $\mu\text{l}/\text{min}$ (based on equipment capability), where the podocyte induction media and the CultureBoost were recirculated in the system and replenished every 2 days. The chips were successfully propagated with cells using either the Emulate system or the more affordable Ismatec peristaltic pump.

Disease modeling

ADR (LC Laboratories, D-4000) was reconstituted in DMSO (Sigma-Aldrich, D2438) to generate a stock solution of 1 mg/ml concentration. ADR medium was prepared by adding 0.5 μl of stock solution and 0.5 μl of DMSO into every 1 ml of CultureBoost to achieve a final ADR concentration of 0.5 $\mu\text{g}/\text{ml}$. DMSO medium (vehicle control) was made by adding 1 μl of DMSO into every 1 ml of CultureBoost to achieve a final DMSO concentration of 0.1% (v/v). ADR medium or DMSO medium were added into the chip's bottom channel inlet media reservoirs, and CultureBoost was added into each chip's top channel inlet media reservoirs. The chips were further perfused for 3 days at 37°C and 5% CO₂.

Molecular filtration assay

Albumin–Texas Red (Thermo Fisher Scientific, A23017) was reconstituted in 1 ml of CultureBoost to prepare an albumin stock solution (5 mg/ml); inulin-FITC (Sigma-Aldrich, F3272) was reconstituted in CultureBoost to prepare an inulin stock solution (7.6 mg/ml), and urea (Sigma-Aldrich, U5378) was reconstituted in sterile water to prepare a urea stock solution (104.24 mg/ml). The albumin, inulin, and urea stock solutions were added to the CultureBoost medium to achieve final concentrations of 100 $\mu\text{g}/\text{ml}$ for albumin, 10 $\mu\text{g}/\text{ml}$ for inulin, and 300 $\mu\text{g}/\text{ml}$ for urea. CultureBoost supplemented with albumin, inulin, and urea was added into all chip bottom channel inlet media reservoirs, and CultureBoost was added into all chip top channel inlet media reservoirs. Media from the outlet media reservoirs were aspirated. The chips were then perfused continuously for 6 hours at 37°C and 5% CO₂. Then, 100 μl of media from the top channel outlet reservoirs and bottom channel inlet reservoirs were collected into a flat clear-bottom black 96-well plate (Corning, CLS3614) in technical replicates with albumin and inulin standard made by serial dilutions of albumin (100 $\mu\text{g}/\text{ml}$) and inulin (10 $\mu\text{g}/\text{ml}$). The fluorescence intensities of all wells were detected using a plate reader (Molecular Devices SpectraMax iD3). Albumin was detected using excitation at 550 nm and emission at 615 nm; inulin was detected using excitation at 513 nm and emission at 557 nm. A urea assay kit (Abcam, ab83362) was used to determine urea concentration. Data in Fig. 2E were generated using the Emulate system, and data in Fig. 2H were generated using the Ismatec peristaltic pump. The data were processed and analyzed using Microsoft Excel 2023 and GraphPad Prism (version 9.5.1.). Clearance (%) was calculated by Eq. 1. As shown below, where $[U]$ is the urinary outflow concentration and $[V]$ is the total vascular stock concentration (8).

$$\text{Clearance (\%)} = \frac{[U]}{[V]} \times 100\% \quad (1)$$

Urea assay kit

Urea concentrations in channel outflow media were determined by using a urea assay kit (Abcam, ab83362). Briefly, the cell culture supernatant was collected from the peristaltic pump outlet media reservoirs and was centrifuged at 1500 rpm for 10 min at 4°C, the resulting supernatant was further diluted twofold, and 50 μl of each sample was added along with the standard dilution (50 μl) into a flat-bottom 96-well plate (Thermo Fisher Scientific, 168055) in technical duplicates. Fifty microliters of CultureBoost without supplements (background control) was included along with the samples and standard dilution and mixed with 50 μl of background reaction mix, and the samples and standards were mixed with 50 μl of reaction mix. The samples, background controls, and standards were then incubated for 1 hour at 37°C. The plate was then immediately analyzed by fluorescence plate reading (Molecular Devices SpectraMax iD3) at 570 nm. The data were processed and analyzed using Microsoft Excel 2023 and GraphPad Prism (version 9.5.1.).

Immunofluorescence microscopy analyses

Cells in the glomerulus bioMF OOC devices were rinsed once with 1× Dulbecco's phosphate-buffered saline (DPBS) (Gibco, 14190144), followed by fixation with 4% paraformaldehyde (Thermo Fisher Scientific, 28908) for 20 min at room temperature. Subsequently, the cells were washed once with 0.125% Triton X-100/DPBS (Triton X-100, Thermo Fisher Scientific, HFH10) for 5 min at room temperature to permeabilize the cells, followed by incubation with 1% bovine serum albumin (BSA) in 0.125% Triton X/DPBS (BSA, Sigma-Aldrich) for 1 hour at room temperature to block unspecific binding. Afterward, the cells were rinsed three times with 0.125% Triton X/DPBS, 5 min at room temperature for each rinse, and then the cells were incubated overnight at 4°C with primary antibodies of interest: anti-nephrin, 1:200 dilution (American Research Products, GPN02); anti-VE-cadherin, 1:200 dilution (Santa Cruz, sc-9989); anti-podocin, 1:200 dilution (Abcam, ab50339); anti-collagen IV, 1:200 dilution (Thermo Fisher Scientific, 14-9871-82), anti-nidogen-1, 1:50 dilution (Thermo Fisher Scientific, MA5-23911); anti-agrin, 1:100 dilution (Thermo Fisher Scientific, PA5-103585); and anti-VEGF-165, 1:20 dilution (Bio-Techne, AF-293-SP). The cells were rinsed three times with 0.125% Triton X/DPBS, 5 min at room temperature for each rinse, and were incubated with the respective secondary antibodies (at 1:1000 dilution) for 1 hour at room temperature, followed by rinsing three times with 1× DPBS and once with distilled water (Gibco, 15230001). The secondary antibodies used in this study were Alexa Fluor (AF) 488 goat anti-guinea pig (Thermo Fisher Scientific, A11073), AF594 donkey anti-mouse (Thermo Fisher Scientific, A21203), AF488 donkey anti-mouse (Thermo Fisher Scientific, A21202), AF594 donkey anti-rabbit (Thermo Fisher Scientific, A21207), AF488 donkey anti-rabbit (Thermo Fisher Scientific, A21206), and AF488 donkey anti-goat (Thermo Fisher Scientific, A11055). The cells were then incubated with 4',6-diamidino-2-phenylindole (DAPI; 1:1000 in distilled water) for 5 min at room temperature, followed by incubation with 0.03% Sudan Black B (Sigma-Aldrich, 199664) in 70% ethanol (VWR, 89125-172) for 5 min at room temperature. Then, the cells were rinsed three times with 1× DPBS and stored in 1× DPBS for immunofluorescence visualization. The cells in the chips were visualized by a Leica SP8 upright

confocal system (Leica), and the z-stack images were processed and analyzed by Fiji ImageJ (version 1.53f51). The 3D-reconstructed image shown in Fig. 2C was captured by flipping the device over to visualize each side separately at the same location, due to the opacity of the SF membrane. Another 3D-reconstructed image obtained without flipping the device over (fig. S2) shows the native proximity of the podocytes and endothelial cells in the bioMF OOC device.

Enzyme-linked immunosorbent assay

An ELISA for VEGF-A was performed using a Human VEGF-A ELISA kit (RayBiotech). Briefly, the cell culture supernatant was collected from the Human Emulation System outlet media reservoirs and was centrifuged at 1500 rpm for 10 min at 4°C, the resulting supernatant was further diluted threefold, and 100 μ l of each sample was added along with the standard dilution (100 μ l) into eight-well strips from the assay kit in technical duplicates. The samples and standards were then incubated for 2.5 hours followed by rinsing four times with 1 \times wash solution, incubation with biotinylated antibody for 1 hour at room temperature, incubation with streptavidin solution for 45 min at room temperature, incubation with TEM One-Step Substrate Reagent for 30 min at room temperature in dark, and then adding Stop Solution. The plate was immediately analyzed by fluorescence plate reading (Molecular Devices Spectra-Max iD3) at 450 nm. The results were processed and analyzed using Microsoft Excel 2023 and GraphPad Prism (version 9.5.1.).

Scanning electron microscopy

For imaging the glomerulus bioMF OOC devices, air-dried chips were sliced using a scalpel (Thermo Fisher Scientific, 08-927-5B) for cross-sectional imaging, and the resulting chip slices (~5-mm thick) and SF/PDMS bottom chips were sputter-coated with gold at 11 mA for 200 s. For imaging PDMS chips, air-dried PDMS chips were sliced and sputter-coated following the same method used for the glomerulus bioMF OOC devices. For PDMS membrane morphological characterization, the PDMS chip top compartment was peeled off, and the resulting exposed PDMS membrane was sputter-coated with gold at 11 mA for 200 s. The resulting chip and PDMS chip samples were visualized using an Apreo S scanning electron microscopy system (Thermo Fisher Scientific) at 2 kV and 25 pA. The images were processed and analyzed by Fiji ImageJ (version 1.53f51).

Transmission electron microscopy

Cells in the chips were rinsed once with 1 \times DPBS, followed by fixation with a fixative solution containing 10 ml of 20% formaldehyde (Sigma-Aldrich, 8.18708), 4 ml of 25% glutaraldehyde (Sigma-Aldrich, G7651), 5 ml of 10 \times phosphate-buffered saline (Gibco, 14200075), and 31 ml of distilled water (Gibco, 15230001), overnight at 4°C or 3 hours at room temperature (~25°C). The samples were postfixed with 1% osmium tetroxide (Electron Microscopy Sciences, 19180) for 1 hour at room temperature in the fume hood, followed by fixation with 0.5% uranyl acetate (Electron Microscopy Sciences, 22400) and dehydration with ethanol (VWR) gradient. The chip's top compartment was then removed, followed by immersion of the resulting chips in the Spurr's resin containing 4.1 g of 3,4-Epoxyhexanemethyl 3,4-epoxycyclohexanecarboxylate (ERL 4221) (Electron Microscopy Sciences, 15004), 5.9 g of Nonenyl Succinic Anhydride (NSA) (Electron Microscopy Sciences, 19050), 1.43 g of Dow epoxy resins (DER) 736 (Electron Microscopy Sciences, 13000), and 0.1 ml of 2-Dimethylaminoethanol (DMAE) (Electron Microscopy Sciences,

13300), overnight at room temperature. Afterward, the chips were immersed in a freshly prepared Spurr's resin and cured at 50° to 60°C for 24 to 48 hours. The resulting chip samples were microtome-sliced after peeling off the bottom PDMS compartment, loaded on TEM grids, counterstained, and visualized using TEM (FEI Tecnai G² Twin). Micrographs were organized using Adobe Illustrator 2023. SF membrane porosity was quantified using Fiji ImageJ (version 1.53f51) by specifically focusing on the center part of the SF membrane (to avoid background signals from the cell layers), as depicted in fig. S4. Endothelial fenestration was quantified using Fiji ImageJ by quantifying the cells in the field of view.

Microstrain analyzer

Young's modulus of the electrospun SF membranes was measured by a microstrain analyzer (TA Instruments) using uniaxial tensile testing. The SF membranes were cut into 5 cm by 0.5 cm rectangles and loaded onto a tension immersion fixture to immerse the SF membrane sample in water at room temperature (25°C) throughout the measurement. The stress-strain curves were obtained at a 100-s testing duration and a 0.47-mm/s uniaxial stretching rate, using $n = 10$ individual samples from two independent SF membrane synthesis sessions. Each sample was measured once. The Young's modulus values were calculated by measuring the slope of the linear region of the stress-strain curves using GraphPad Prism software (version 9.5.1.).

Attenuated total reflectance accessory—FTIR spectroscopy

FTIR spectroscopy analysis of the electrospun SF membrane was performed using a Thermo Electron Nicolet 8700 (Thermo Fisher Scientific) with an attenuated total reflectance accessory. All spectra were obtained in absorbance mode on a Ge crystal at a resolution of 4 cm^{-1} with 32 scans and a spectral range of 500 to 2000 cm^{-1} . The background spectrum was acquired by using a piece of bare non-stick aluminum foil before sampling. For each sample, three different locations were measured, and a total of three independent samples were measured for quantification and to assess reproducibility. For each sample, the average values of three measured locations were used for the absorption peak analysis using GraphPad Prism software (version 9.5.1.).

Statistical analysis

All data were presented as mean \pm SD. To compare two groups with one variable, the data were analyzed using unpaired two-tailed Student's *t* test analysis with a 95% confidence interval. Differences were considered significant at $*P \leq 0.05$, $**P \leq 0.01$, and $***P \leq 0.001$. All statistical analyses were performed in GraphPad Prism software (version 9.5.1.).

Supplementary Materials

This PDF file includes:

Figs. S1 to S9

Table S1

Legend for movie S1

Other Supplementary Material for this manuscript includes the following:

Movie S1

REFERENCES AND NOTES

1. C. M. Leung, P. De Haan, K. Ronaldson-Bouchard, G.-A. Kim, J. Ko, H. S. Rho, Z. Chen, P. Habibovic, N. L. Jeon, S. Takayama, A guide to the organ-on-a-chip. *Nat. Rev. Methods Primers* **2**, 33 (2022).

2. A. E. Danku, E.-H. Dulf, C. Braicu, A. Jurj, I. Berindan-Neagoe, Organ-on-a-chip: A survey of technical results and problems. *Front. Bioeng. Biotechnol.* **10**, 840674 (2022).
3. D. Singh, A. Mathur, S. Arora, S. Roy, N. Mahindroo, Journey of organ on a chip technology and its role in future healthcare scenario. *Appl. Surf. Sci.* **9**, 100246 (2022).
4. Q. Wu, J. Liu, X. Wang, L. Feng, J. Wu, X. Zhu, W. Wen, X. Gong, Organ-on-a-chip: Recent breakthroughs and future prospects. *Biomed. Eng. Online* **19**, 9 (2020).
5. M. G. Bonner, H. Gudapati, X. Mou, S. Musah, Microfluidic systems for modeling human development. *Development* **149**, dev199463 (2022).
6. T.-E. Park, N. Mustafaoglu, A. Herland, R. Hasselkus, R. Mannix, E. A. FitzGerald, R. Prantil-Baun, A. Watters, O. Henry, M. Benz, Hypoxia-enhanced blood-brain barrier chip recapitulates human barrier function and shuttling of drugs and antibodies. *Nat. Commun.* **10**, 2621 (2019).
7. D. Huh, D. C. Leslie, B. D. Matthews, J. P. Fraser, S. Jurek, G. A. Hamilton, K. S. Thorneleo, M. A. McAlexander, D. E. Ingber, A human disease model of drug toxicity-induced pulmonary edema in a lung-on-a-chip microdevice. *Sci. Transl. Med.* **4**, 159ra147 (2012).
8. S. Musah, A. Mammoto, T. C. Ferrante, S. S. F. Jeanty, M. Hirano-Kobayashi, T. Mammoto, K. Roberts, S. Chung, R. Novak, M. Ingram, T. Fatanat-Didar, S. Koshy, J. C. Weaver, G. M. Church, D. E. Ingber, Mature induced-pluripotent-stem-cell-derived human podocytes reconstitute kidney glomerular-capillary-wall function on a chip. *Nat. Biomed. Eng.* **1**, 0069 (2017).
9. S. Musah, N. Dimitrakakis, D. M. Camacho, G. M. Church, D. E. Ingber, Directed differentiation of human induced pluripotent stem cells into mature kidney podocytes and establishment of a Glomerulus Chip. *Nat. Protoc.* **13**, 1662–1685 (2018).
10. Y. Roye, R. Bhattacharya, X. Mou, Y. Zhou, M. A. Burt, S. Musah, A personalized glomerulus chip engineered from stem cell-derived epithelium and vascular endothelium. *Micromachines* **12**, 967 (2021).
11. T. D. Kalejaiye, J. A. Holmes, R. Bhattacharya, S. Musah, "Reconstitution of the kidney glomerular capillary wall" in *Regenerative Nephrology* (Elsevier, 2022), pp. 331–351.
12. D. T. Phan, X. Wang, B. M. Craver, A. Sobrinho, D. Zhao, J. C. Chen, L. Y. Lee, S. C. George, A. P. Lee, C. C. Hughes, A vascularized and perfused organ-on-a-chip platform for large-scale drug screening applications. *Lab Chip* **17**, 511–520 (2017).
13. A. D. Barreto, M. A. Burt, S. Musah, Advancing drug discovery for glomerulopathies using stem-cell-derived kidney models. *Trends Pharmacol. Sci.* **44**, 204–207 (2023).
14. J. Wang, C. Wang, N. Xu, Z.-F. Liu, D.-W. Pang, Z.-L. Zhang, A virus-induced kidney disease model based on organ-on-a-chip: Pathogenesis exploration of virus-related renal dysfunctions. *Biomaterials* **219**, 119367 (2019).
15. T. D. Kalejaiye, A. D. Barreto, S. Musah, Translating organoids into artificial kidneys. *Curr. Transplant. Rep.* **9**, 276–286 (2022).
16. D. Huh, B. D. Matthews, A. Mammoto, M. Montoya-Zavala, H. Y. Hsin, D. E. Ingber, Reconstituting organ-level lung functions on a chip. *Science* **328**, 1662–1668 (2010).
17. D. Sun, W. Gao, H. Hu, S. Zhou, Why 90% of clinical drug development fails and how to improve it? *Acta Pharm Sin B* **12**, 3049–3062 (2022).
18. N. Franzen, W. H. van Harten, V. P. Retèl, P. Loskill, J. van den Eijnden-van Raaij, M. IJzerman, Impact of organ-on-a-chip technology on pharmaceutical R&D costs. *Drug Discov. Today* **24**, 1720–1724 (2019).
19. C. Ma, Y. Peng, H. Li, W. Chen, Organ-on-a-chip: A new paradigm for drug development. *Trends Pharmacol. Sci.* **42**, 119–133 (2021).
20. M. Wadman, FDA no longer has to require animal testing for new drugs. *Science* **379**, 127–128 (2023).
21. H. J. Kim, D. Huh, G. Hamilton, D. E. Ingber, Human gut-on-a-chip inhabited by microbial flora that experiences intestinal peristalsis-like motions and flow. *Lab Chip* **12**, 2165–2174 (2012).
22. V. Kappings, C. Grün, D. Ivannikov, I. Hebeiss, S. Kattge, I. Wendland, B. E. Rapp, M. Hettel, O. Deutschmann, U. Schepers, vasQchip: A novel microfluidic, artificial blood vessel scaffold for vascularized 3D tissues. *Adv. Mater. Technol.* **3**, 1700246 (2018).
23. C. Chew, R. Lennon, Basement membrane defects in genetic kidney diseases. *Front. Pediatr.* **6**, 11 (2018).
24. C. B. Marshall, Rethinking glomerular basement membrane thickening in diabetic nephropathy: Adaptive or pathogenic? *Am. J. Physiol. Renal. Physiol.* **311**, F831–F843 (2016).
25. W. Quirós-Solano, N. Gaio, O. Stassen, Y. Arik, C. Silvestri, N. Van Engeland, A. Van der Meer, R. Passier, C. Sahlgren, C. Bouten, A. van den Berg, R. Dekker, P. M. Sarro, Microfabricated tuneable and transferable porous PDMS membranes for Organs-on-Chips. *Sci. Rep.* **8**, 13524 (2018).
26. C. H. Seo, K. Furukawa, K. Montagne, H. Jeong, T. Ushida, The effect of substrate microtopography on focal adhesion maturation and actin organization via the RhoA/ROCK pathway. *Biomaterials* **32**, 9568–9575 (2011).
27. Y. Cheng, G. Cheng, C. Xie, C. Yin, X. Dong, Z. Li, X. Zhou, Q. Wang, H. Deng, Z. Li, Biomimetic silk fibroin hydrogels strengthened by silica nanoparticles distributed nanofibers facilitate bone repair. *Adv. Healthc. Mater.* **10**, e2001646 (2021).
28. J. Chen, Y. Zhan, Y. Wang, D. Han, B. Tao, Z. Luo, S. Ma, Q. Wang, X. Li, L. Fan, Chitosan/silk fibroin modified nanofibrous patches with mesenchymal stem cells prevent heart remodeling post-myocardial infarction in rats. *Acta Biomater.* **80**, 154–168 (2018).
29. G. Cheng, Z. Davoudi, X. Xing, X. Yu, X. Cheng, Z. Li, H. Deng, Q. Wang, Advanced silk fibroin biomaterials for cartilage regeneration. *ACS Biomater. Sci. Eng.* **4**, 2704–2715 (2018).
30. L. Lamboni, M. Gauthier, G. Yang, Q. Wang, Silk sericin: A versatile material for tissue engineering and drug delivery. *Biotechnol. Adv.* **33**, 1855–1867 (2015).
31. N. J. Prakash, P. P. Mane, S. M. George, B. Kandasubramanian, Silk fibroin as an immobilization matrix for sensing applications. *ACS Biomater. Sci. Eng.* **7**, 2015–2042 (2021).
32. H. Yin, Y. Zhou, J. Xu, S. Ai, L. Cui, L. Zhu, Amperometric biosensor based on tyrosinase immobilized onto multiwalled carbon nanotubes-cobalt phthalocyanine-silk fibroin film and its application to determine bisphenol A. *Anal. Chim. Acta* **659**, 144–150 (2010).
33. S. Kaushik, P. D. Thungon, P. Goswami, Silk fibroin: An emerging biocompatible material for application of enzymes and whole cells in bioelectronics and bioanalytical sciences. *ACS Biomater. Sci. Eng.* **6**, 4337–4355 (2020).
34. D. N. Rockwood, R. C. Preda, T. Yücel, X. Wang, M. L. Lovett, D. L. Kaplan, Materials fabrication from Bombyx mori silk fibroin. *Nat. Protoc.* **6**, 1612–1631 (2011).
35. S. Enomoto, M. Sumi, K. Kajimoto, Y. Nakazawa, R. Takahashi, C. Takabayashi, T. Asakura, M. Sata, Long-term patency of small-diameter vascular graft made from fibroin, a silk-based biodegradable material. *J. Vasc. Surg.* **51**, 155–164 (2010).
36. V. Catto, S. Farè, I. Cattaneo, M. Figliuzzi, A. Alessandrino, G. Freddi, A. Remuzzi, M. C. Tanzi, Small diameter electrospun silk fibroin vascular grafts: Mechanical properties, in vitro biodegradability, and in vivo biocompatibility. *Mater. Sci. Eng. C* **54**, 101–111 (2015).
37. E. Servoli, D. Maniglio, A. Motta, R. Predazzer, C. Migliaresi, Surface properties of silk fibroin films and their interaction with fibroblasts. *Macromol. Biosci.* **5**, 1175–1183 (2005).
38. G. Li, K. Chen, D. You, M. Xia, W. Li, S. Fan, R. Chai, Y. Zhang, H. Li, S. Sun, Laminin-coated electrospun regenerated silk fibroin mats promote neural progenitor cell proliferation, differentiation, and survival in vitro. *Front. Bioeng. Biotechnol.* **7**, 190 (2019).
39. G. Zhao, X. Zhang, B. Li, G. Huang, F. Xu, X. Zhang, Solvent-free fabrication of carbon nanotube/silk fibroin electrospun matrices for enhancing cardiomyocyte functionalities. *ACS Biomater. Sci. Eng.* **6**, 1630–1640 (2020).
40. L. Huang, W. Yuan, Y. Hong, S. Fan, X. Yao, T. Ren, L. Song, G. Yang, Y. Zhang, 3D printed hydrogels with oxidized cellulose nanofibers and silk fibroin for the proliferation of lung epithelial stem cells. *Cellul.* **28**, 241–257 (2021).
41. X. Mou, J. Shah, R. Bhattacharya, T. D. Kalejaiye, B. Sun, P.-C. Hsu, S. Musah, A biomimetic electrospun membrane supports the differentiation and maturation of kidney epithelium from human stem cells. *Bioengineering* **9**, 188 (2022).
42. F. Sun, D. Xiao, H. Su, Z. Chen, B. Wang, X. Feng, Z. Mao, X. Sui, Highly stretchable porous regenerated silk fibroin film for enhanced wound healing. *J. Mater. Chem. B* **11**, 1486–1494 (2023).
43. A. Karimi, A. Shojaei, Measurement of the mechanical properties of the human kidney. *IRBM* **38**, 292–297 (2017).
44. E. Tanzli, A. Ehrmann, Electrospun nanofibrous membranes for tissue engineering and cell growth. *Appl. Sci.* **11**, 6929 (2021).
45. W. Cui, Y. Zhou, J. Chang, Electrospun nanofibrous materials for tissue engineering and drug delivery. *Sci. Technol. Adv. Mater.* **11**, 014108 (2010).
46. L. Liverani, V. Guarino, V. La Carrubba, A. Boccaccini, "Porous biomaterials and scaffolds for tissue engineering" in *Encyclopedia of biomedical engineering* (Elsevier, 2019), vol. 1, pp. 188–202.
47. E. Davison-Kotler, W. S. Marshall, E. García-Gareta, Sources of collagen for biomaterials in skin wound healing. *Bioengineering* **6**, 56 (2019).
48. A. B. Allen, L. B. Priddy, M.-T. A. Li, R. E. Goldberg, Functional augmentation of naturally-derived materials for tissue regeneration. *Ann. Biomed. Eng.* **43**, 555–567 (2015).
49. B. N. Brown, S. F. Badylak, Extracellular matrix as an inductive scaffold for functional tissue reconstruction. *Transl. Res.* **163**, 268–285 (2014).
50. J. Reiser, M. M. Altintas, Podocytes. *F1000Res.* **5**, 114 (2016).
51. V. Ruotsalainen, P. Ljungberg, J. Wartiovaara, U. Lenkkeri, M. Kestilä, H. Jalanko, C. Holmberg, K. Tryggvason, Nephin is specifically located at the slit diaphragm of glomerular podocytes. *Proc. Natl. Acad. Sci. U.S.A.* **96**, 7962–7967 (1999).
52. K. Schwarz, M. Simons, J. Reiser, M. A. Saleem, C. Faul, W. Kriz, A. S. Shaw, L. B. Holzman, P. Mundel, Podocin, a raft-associated component of the glomerular slit diaphragm, interacts with CD2AP and nephrin. *J. Clin. Invest.* **108**, 1621–1629 (2001).
53. D. Vestweber, VE-Cadherin. *Arterioscler. Thromb. Vasc. Biol.* **28**, 223–232 (2008).
54. L. Ning, H. Y. Suleiman, J. H. Miner, Synaptopodin is dispensable for normal podocyte homeostasis but is protective in the context of acute podocyte injury. *J. Am. Soc. Nephrol.* **31**, 2815–2832 (2020).
55. J. H. Miner, The glomerular basement membrane. *Exp. Cell Res.* **318**, 973–978 (2012).
56. R. Botev, J.-P. Mallié, C. Couchoud, O. Schück, J.-P. Fauvel, J. F. Wetzels, N. Lee, N. G. De Santo, M. Cirillo, Estimating glomerular filtration rate: Cockcroft-Gault and modification of diet in renal disease formulas compared to renal inulin clearance. *Clin. J. Am. Soc. Nephrol.* **4**, 899–906 (2009).
57. J. Peti-Peterdi, A. Sipos, A high-powered view of the filtration barrier. *J. Am. Soc. Nephrol.* **21**, 1835–1841 (2010).

58. A. Tojo, S. Kinugasa, Mechanisms of glomerular albumin filtration and tubular reabsorption. *Int. J. Nephrol.* **2012**, 481520 (2012).
59. W. Barmore, F. Azad, W. L. Stone, Physiology, urea cycle. (2018).
60. H. K. Groves, H. T. Lee, "19 - Perioperative Management of Renal Failure and Renal Transplant" in *Perioperative Medicine (Second Edition)*, M. F. Newman, L. A. Fleisher, C. Ko, M. Mythen, Eds. (Elsevier, 2022), pp. 259–275.
61. J. T. Daugirdas, T. A. Depner, J. Inrig, R. Mehrotra, M. V. Rocco, R. S. Suri, D. E. Weiner, N. Greer, A. Ishani, R. MacDonald, KDOQI clinical practice guideline for hemodialysis adequacy: 2015 update. *Am. J. Kidney Dis.* **66**, 884–930 (2015).
62. G. S. Markowitz, A. S. Bombback, M. A. Perazella, Drug-induced glomerular disease: Direct cellular injury. *Clin. J. Am. Soc. Nephrol.* **10**, 1291–1299 (2015).
63. C.-K. Chiang, R. Inagi, Glomerular diseases: Genetic causes and future therapeutics. *Nat. Rev. Nephrol.* **6**, 539–554 (2010).
64. T. D. Kalejaiye, R. Bhattacharya, M. A. Burt, T. Travieso, A. E. Okafor, X. Mou, M. Blasi, S. Musah, SARS-CoV-2 employ BSG/CD147 and ACE2 receptors to directly infect human induced pluripotent stem cell-derived kidney podocytes. *Front. Cell Dev. Biol.* **10**, 855340 (2022).
65. T. D. Kalejaiye, R. Bhattacharya, M. A. Burt, T. Travieso, A. E. Okafor, X. Mou, M. Blasi, S. Musah, SARS-CoV-2 employ BSG/CD147 and ACE2 receptors facilitate SARS-CoV-2 infection of human iPSC cell-derived kidney podocytes. *bioRxiv* 2021.11.16.468893 (2021).
66. R. Kazancıoğlu, Risk factors for chronic kidney disease: An update. *Kidney. Int. Suppl.* **3**, 368–371 (2013).
67. S. Ayla, I. Seckin, G. Tanriverdi, M. Cengiz, M. Eser, B. Soner, G. Oktem, Doxorubicin induced nephrotoxicity: Protective effect of nicotinamide. *Int. J. Cell Biol.* **2011**, 390238 (2011).
68. V. W. Lee, D. C. Harris, Adriamycin nephropathy: A model of focal segmental glomerulosclerosis. *Nephrol. Ther.* **16**, 30–38 (2011).
69. M. A. Burt, T. D. Kalejaiye, R. Bhattacharya, N. Dimitrakakis, S. Musah, Adriamycin-induced podocyte injury disrupts the YAP-TEAD1 axis and downregulates Cyr61 and CTGF expression. *ACS Chem. Biol.* **17**, 3341–3351 (2022).
70. J. Gupta, N. Mitra, P. A. Kanetsky, J. Devaney, M. R. Wing, M. Reilly, V. O. Shah, V. S. Balakrishnan, N. J. Guzman, M. Girndt, B. G. Periera, H. I. Feldman, J. W. Kusek, M. M. Joffe, D. S. Raj; CRIC Study Investigators, Association between albuminuria, kidney function, and inflammatory biomarker profile in CKD in CRIC. *Clin. J. Am. Soc. Nephrol.* **7**, 1938–1946 (2012).
71. C. Zoja, P. B. Garcia, C. Rota, S. Conti, E. Gagliardini, D. Corna, C. Zanchi, P. Bigini, A. Benigni, G. Remuzzi, M. Morigi, Mesenchymal stem cell therapy promotes renal repair by limiting glomerular podocyte and progenitor cell dysfunction in adriamycin-induced nephropathy. *Am. J. Physiol. Renal. Physiol.* **303**, F1370–F1381 (2012).
72. I. Grgic, C. R. Brooks, A. F. Hofmeister, V. Bijol, J. V. Bonventre, B. D. Humphreys, Imaging of podocyte foot processes by fluorescence microscopy. *J. Am. Soc. Nephrol.* **23**, 785–791 (2012).
73. K. P. Arkill, K. Qvortrup, T. Starborg, J. M. Mantell, C. Knupp, C. C. Michel, S. J. Harper, A. H. Salmon, J. M. Squire, D. O. Bates, C. R. Neal, Resolution of the three dimensional structure of components of the glomerular filtration barrier. *BMC Nephrol.* **15**, 24 (2014).
74. S. C. Satchell, F. Braet, Glomerular endothelial cell fenestrations: An integral component of the glomerular filtration barrier. *Am. J. Physiol. Renal. Physiol.* **296**, F947–F956 (2009).
75. J. Nguyen, Y.-Y. Lin, S. Gerecht, The next generation of endothelial differentiation: Tissue-specific ECs. *Cell Stem Cell* **28**, 1188–1204 (2021).
76. Y. Z. Zhang, H. S. Lee, Quantitative changes in the glomerular basement membrane components in human membranous nephropathy. *J. Pathol.* **183**, 8–15 (1997).
77. R. R. Watson, V. R. Preedy, Bioactive food as dietary interventions for diabetes (Academic Press, 2019).
78. S. Sethi, F. C. Fervenza, Y. Zhang, R. J. Smith, Secondary focal and segmental glomerulosclerosis associated with single-nucleotide polymorphisms in the genes encoding complement factor H and C3. *Am. J. Kidney Dis.* **60**, 316–321 (2012).
79. L. Atchison, N. O. Abutaleb, E. Snyder-Mounts, Y. Gete, A. Ladha, T. Ribar, K. Cao, G. A. Truskey, iPSC-derived endothelial cells affect vascular function in a tissue-engineered blood vessel model of Hutchinson-Gilford progeria syndrome. *Stem Cell Reports* **14**, 325–337 (2020).
80. I. Kamenetsky, R. M. Rangayyan, H. Benediktsson, Analysis of the glomerular basement membrane in images of renal biopsies using the split-and-merge method: a pilot study. *J. Digit. Imaging* **23**, 463–474 (2010).

Acknowledgments: We thank P.-C. Hsu from the Department of Mechanical Engineering and Material Science at Duke University (now at Pritzker School of Molecular Engineering at University of Chicago), M. Becker from the Department of Chemistry at Duke University for providing the electrospinning equipment, and Musah Lab members T. Kalejaiye, R. Bhattacharya, A. Barreto, and Y. Zhang for technical assistance. We also thank H. Leddy, L. Parks, K. Bryson, J. Dalton, and all staff members at Duke SMIF for technical assistance with TEM sample embedding and device microfabrication. **Funding:** This work was funded by a Whitehead Scholarship in Biomedical Research, Chair's Research Award from the Department of Medicine at Duke University, MEDx Pilot Grant on Biomechanics in Injury or injury repair, Burroughs Wellcome Fund PDEP Career Transition Ad Hoc Award, Duke Incubation Fund from the Duke Innovation & Entrepreneurship Initiative, a Genentech Research Award, a George M. O'Brien Kidney Center Pilot Grant (P30 DK081943), and an NIH Director's New Innovator Grant (award number DP2DK139544) awarded to S.M. This work was performed in part at the Duke University SMIF, a member of the North Carolina Research Triangle Nanotechnology Network (RTNN), which is supported by the National Science Foundation (award number ECCS-2025064) as part of the National Nanotechnology Coordinated Infrastructure (NNCI). X.M. is a recipient of a graduate research fellowship from the International Foundation for Ethical Research (IFER). **Author contributions:** Conceptualization: S.M. Methodology: S.M., X.M., and J.S. Data curation: X.M., J.S., and C.D. Data interpretation: X.M. and S.M. Validation: X.M., J.S., C.D., and Y.R. Investigation: X.M., J.S., Y.R., and C.D. Formal analysis: X.M., J.S., Y.R., and C.D. Resources: S.M. Visualization: X.M., J.S., and C.D. Writing (original draft): X.M. Writing (reviewing): S.M., X.M., J.S., Y.R., and C.D. Writing (editing): S.M. Project administration: S.M. Supervision: S.M. Funding acquisition: S.M. **Competing interests:** S.M. is an inventor on a patent (US20210338736A1) for stem cell differentiation into podocytes, held by Harvard College. S.M. and X.M. are coinventors on a pending patent application (USPTO application number 64/506190) for the development of a biomaterial membrane for tissue engineering and biomedical applications, held by Duke University. The other authors declare they have no competing interests. **Data and materials availability:** All data needed to evaluate the conclusions in the paper are present in the paper and/or the Supplementary Materials. All reagents generated in this study are accessible from the corresponding author upon reasonable request and with an institutionally approved material transfer agreement.

Submitted 1 December 2023

Accepted 30 April 2024

Published 5 June 2024

10.1126/sciadv.adn2689